Proximity-induced spin-polarized magnetocaloric effect in transition metal dichalcogenides

Natalia Cortés [1,*] Francisco J. Peña [1] Oscar Negrete [1,2] and Patricio Vargas [1,2]

[1]*Departamento de Física, Universidad Técnica Federico Santa María, Casilla 110V, Valparaíso, Chile*
[2]*Centro para el Desarrollo de la Nanociencia y la Nanotecnología, 8320000 Santiago, Chile*

We explore proximity-induced magnetocaloric effect (MCE) on transition metal dichalcogenides, focusing on a two-dimensional (2D) MoTe$_2$ monolayer deposited on a ferromagnetic semiconductor EuO substrate connected to a heat source. We model this heterostructure using a tight-binding model, incorporating exchange, and Rashba fields induced by proximity to EuO and including temperature through Fermi statistics and mean-field calculations. The MCE is induced on the 2D MoTe$_2$ layer due to the EuO substrate, revealing large spin-polarized entropy changes for energies out of the band gap of the MoTe$_2$-EuO system. By gating the chemical potential, the MCE can be tuned to produce heating for spin up and cooling for spin down across the K- and K'-valley splitting in the valence band, whereas heats for both spins in the conduction band up to the EuO Curie temperature. The Rashba field enhances the MCE in the valence zone whereas decreasing it in the conduction bands. The exchange field-induced MCE could be useful to produce tunable spin-polarized thermal responses in magnetic proximitized 2D materials.

I. INTRODUCTION

The magnetic proximity effect takes place when the magnetization of a magnetic crystal is induced on a neighboring nonmagnetic material [1]. Diverse nonmagnetic materials are used to react to the induced magnetism, but considerable attention is lately given to atomically thin two-dimensional (2D) layers [2–4]. The thinness of 2D layers allows for short-range induced magnetism, driving to modifications in the combined electronic states [1] as seen in the band-structure responses. One attractive class of 2D materials that can be mixed with magnetic crystals to produce magnetic proximity effects include transition metal dichalcogenides (TMDs) of the semiconducting MX_2 family ($M =$ Mo and W; $X =$ S, Se, and Te) [5]. The intrinsic lack of inversion symmetry and spin-orbit coupling (SOC) in TMDs cause a sizable spin splitting at the valence-band edges of the spin-valley coupled K and K'—degenerated, yet inequivalent—valleys in the Brillouin zone (BZ) [6], which are related each other by time-reversal symmetry (TRS) [7].

Valley splitting to encode information requires lifting the degeneracy of K and K' TMD valleys, which can be achieved due to broken TRS by either an external magnetic field [8] or induced magnetic exchange fields (MEFs) driven by ferromagnetic substrates [9–12]; however, the resulting valley splittings because of the former are small ($\simeq 0.1$-0.2 meV/T) [13,14]. The induced MEFs on 2D TMDs may have some advantages over large external magnetic fields needed to break TRS and achieve valley polarization. For example, a giant valley splitting (300 meV) at zero K was predicted for MoTe$_2$-EuO [15], a large valley splitting of 16 meV/T at a

temperature of 7 K has been experimentally obtained due to the induced MEF in a WS$_2$-EuS heterostructure [16], and a valley splitting of $\simeq 3.5$ meV was measured in WSe$_2$-CrI$_3$ at 5 K. As one can note, the thermal conditions of typical van der Waals experiments clearly play an important role, as the valley splittings of the proximitized TMDs show large dependence on the Curie temperature of the magnetic substrates [10].

Entropy is a useful fundamental thermodynamic quantity intimately related to temperature and accounting for the number of accessible states of a system. When a material is at constant temperature, and subjected to external magnetic-field changes, it experiences entropy changes, and the magnetocaloric effect (MCE) arises cooling or heating the sample [17–19]. The MCE has been analyzed in diverse magnetic structures [20], including a spin-gapped material [21], a one-dimensional spin-1/2 system [22], frustrated magnets [23], spin-1/2 2D lattices [24], nanomagnets [25], and superlattices showing large entropy changes due to exchange interactions [26]. In 2D layers of graphene and gold, the MCE shows an oscillatory behavior [27,28], and an external magnetic field is capable to control the entropy in TMDs [29]. The MCE has also been reported in bulk EuS [30] and EuO [31] as well as in EuO thin films [32], finding maxima entropy changes near the Curie temperature of each ferromagnet.

We propose here a MCE associated with changes of the induced EuO MEF on MoTe$_2$ driving to large entropy changes. The strength of the induced MEF could be modulated through van der Waals engineering of proximitized materials [10] via nonmagnetic spacer layers [9] or through biaxial strain [33]. Time-reversal symmetry breaking on MoTe$_2$ due to the MEF causes spin-polarized entropy production [34,35], then a spin-polarized MCE can be generated in the valley splitting energy zones. The MoTe$_2$-EuO heterostructure is modeled by a three-orbital tight-binding (3OTB) model, and the MCE is derived
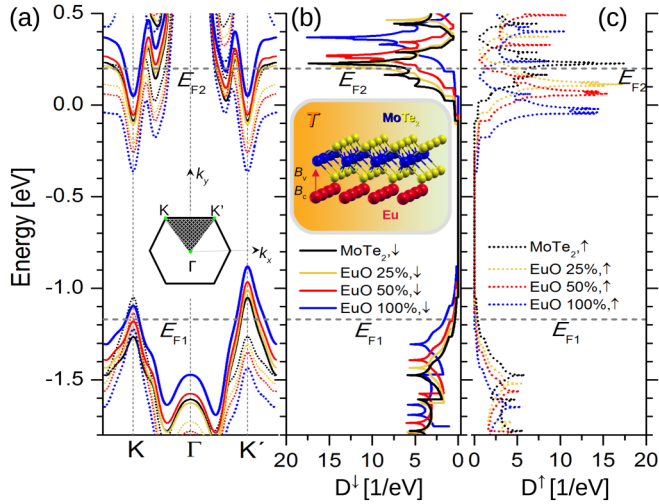
*natalia.cortesm@usm.cl

FIG. 1. (a) K-Γ-K' band structure for suspended MoTe$_2$ mono-layer (black lines) and MoTe$_2$-EuO with $\lambda_R = 0$ (yellow 25%, red 50%, and blue 100% of B_v and B_c). $\Gamma = (0,0)$, $K = \frac{2\pi}{3a}(-1, \sqrt{3})$, and $K' = \frac{2\pi}{3a}(1, \sqrt{3})$ with $a = 3.56$ Å the 2D MoTe$_2$ lattice constant. Spin-polarized density of states (DOS) (b) $D^\downarrow$ and (c) $D^\uparrow$. The inset in (a) shows the BZ for MoTe$_2$-EuO, the shaded area indicates where the DOS is calculated in (b) and (c). The inset in (b) shows a schematic of MoTe$_2$-EuO enclosed by a thermal source at temperature T. Horizontal dashed lines indicate two selected Fermi levels $E_{F1} = -1.17$ and $E_{F2} = 0.2$ eV where we obtain the MCE.

from Fermi statistic and mean-field calculations. The former method considers temperature-independent MEFs, whereas the latter allows to estimate temperature-dependent MEFs to obtain the MCE. For both approaches, we find that when the Fermi energy is tuned along the K and K' valleys of the valence band, the MoTe$_2$-EuO system is able to heat for spin up and cools for spin down, whereas heats for both spins in the conduction band up to the Curie temperature of EuO. We also analyze the effect of the Rashba field within the Fermi-Dirac method, showing that it enhances the cooling effects in the valence band. The generic existence of spin-polarized TMD electronic states given by TRS breaking that can be accessed by gating, suggest that these hybrid systems could be used as tunable thermal spin filters [36] for functional applications considering the anomalous Hall effect [37] as a possible plat-form to produce the induced MCE.

II. QUANTUM-THERMODYNAMIC MODEL

To describe the low-energy spectrum and MCE of the MoTe$_2$-EuO heterostructure [15,38], we use a 3OTB model [39] to include MEF effects. The model has relevant lattice symmetries and has been proven to reliably describe TMDs on diverse situations on magnetic substrates [40–42], induced magnetic interactions, [43,44], and heterostructures [45]. The nearly commensuration of MoTe$_2$-EuO(111) [15,46] (2.7% lattice mismatch), incorporates the substrate effects into the pristine MoTe$_2$ as on-site magnetic exchange [see the inset of Fig. 1(b)] and Rashba fields on the Mo atoms as

$$\mathcal{H}_{\text{MoTe}_2\text{-EuO}} = \mathcal{H}_{\text{MoTe}_2} + \mathcal{H}_{\text{ex}} + \mathcal{H}_R. \quad (1)$$

$\mathcal{H}_{\text{MoTe}_2}$ is the pristine $2H$ phase TMD Hamiltonian [39], including intrinsic SOC and a matrix of hoppings considering next-nearest neighbors (NNNs), it is writ-ten in a basis of relevant transition metal d-orbitals $\{|d_{z^2}, s_z\rangle, |d_{xy}, s_z\rangle, |d_{x^2-y^2}, s_z\rangle\}$ with spin-z component $s_z = \uparrow$, $\downarrow$ [39]. The induced MEF is spin diagonal with blocks $\mathcal{H}_{\text{ex},(\uparrow\uparrow)} = -\mathcal{H}_{\text{ex},(\downarrow\downarrow)} = \text{diag}\{-B_c, -B_v, -B_v\}$, where $B_c = 206$ and $B_v = 170$ meV correspond to conduction and va-lence exchange fields, respectively. Figure 1(a) shows the spin-polarized band structure from Eq. (1) for the suspended MoTe$_2$ 2D monolayer ($\mathcal{H}_{\text{ex}} = \mathcal{H}_R = 0$), and MoTe$_2$-EuO with $\mathcal{H}_R = 0$ and different values of the exchange fields. The MEF breaks TRS, yielding large valley splittings in the valence and conduction bands [15,33], decreasing it as the MEF strength reduces. The Rashba Hamiltonian $\mathcal{H}_R$ in Eq. (1) is given by antidiagonal blocks, mixing the spin and orbital components in the MoTe$_2$ monolayer with coupling $\lambda_R = 72$ meV. All parameters are obtained from density functional theory (DFT) calculations [15,39], see the Appendix for an analysis of the 3OTB in comparison to DFT. We first analyze the MCE for different values of the EuO MEFs and vanishing Rashba cou-pling ($\lambda_R = 0$) after that we include the Rashba effect for the MCE whitin the Fermi-Dirac statistics, then we calcu-late the MCE using a mean-field approximation as we will see later.

In order to correlate both the 3OTB model and the MCE, we numerically calculate the spin-polarized DOS D^{s_z} using a 2D BZ, i.e., $k_z = 0$ in reciprocal k space. We use a fine mesh of about 10×10^6 of k points in the shaded area of the BZ [inset of Fig. 1(a)]. For every k state, we evaluate the eigenvalues from each band of the Hamiltonian of Eq. (1). The DOS $D^{s_z}(E, B_v, B_c)$ depends on the eigenvalue with energy E, and both exchange fields B_v, B_c induced on the MoTe$_2$ monolayer. Figures 1(b) and 1(c) show $D^{s_z}(E, B_v, B_c)$ for the suspended MoTe$_2$ monolayer and MoTe$_2$-EuO system. Note that for the suspended MoTe$_2$, the DOS are equiv-alent, i.e., $D^\uparrow(E, 0, 0) = D^\downarrow(E, 0, 0)$ (as expected from a nonmagnetic material), whereas $D^\uparrow$ ($D^\downarrow$) is downward (up-ward) shifted from the suspended MoTe$_2$ DOS because of the induced MEFs.

The total spin-polarized entropy $S_{\text{tot}}^{s_z} = S_{\text{lat}}(T) + S_{eM}^{s_z}(B_v, B_c, T)$ includes two terms, the entropy of the lattice $S_{\text{lat}}(T)$, giving account of the phonon contribution where we assume it is only dependent on T; and the electromagnetic entropy $S_{eM}^{s_z}$ coming from the full Hamiltonian of Eq. (1), and depending on the exchange fields and temperature. The electromagnetic entropy reads

$$S_{eM}^{s_z}(B_v, B_c, T) = -k_B \int_{E_l}^{E_h} D^{s_z}(E, B_v, B_c)\mathcal{F}(n_F)dE, \quad (2)$$

with $E_{l(h)}$ as the energy of the lowest (highest) occupied electronic eigenvalue. The probability of occupation of each eigenvalue is given by the Fermi-Dirac function distribution $n_F(E, T, \mu) = 1/[e^{\beta(E-\mu)} + 1]$ with $\beta = 1/k_B T$, k_B as the Boltzmann constant, μ as the chemical potential, and T as the heat-source temperature. In Eq. (2),

$$\mathcal{F}(n_F) = n_F \ln n_F + (1 - n_F)\ln(1 - n_F) \quad (3)$$

is approximated by a Lorentzian-like function $L(E, T, \mu) = C/[e^{(|E-\mu|/2k_B T)^{3/2}} + 1]$. By considering low- and high-T values and $C = 1.4$, we obtain excellent agreement between Eq. (3) and $L(E, T, \mu)$ with $-\mathcal{F}(n_F) \approx L(E, T, \mu)$. Note that this approximation can be applied to other quasi-2D materials because L is a generic function depending on the system's eigenenergies E, μ, and T as demonstrated, for example, in Ref. [47]. Therefore Eq. (2) transforms as

$$S_{eM}^{s_z}(B_v, B_c, T) \simeq k_B \int_{E_l}^{E_h} D^{s_z}(E, B_v, B_c)L(E, T, \mu)dE. \quad (4)$$

The main contribution of $L(E, T, \mu)$ to $S_{eM}^{s_z}$ is given by their temperature-dependent width, capturing more available states of the DOS as temperature increases. As revealed in Eq. (4), $S_{eM}^{s_z}$ is the link between the electronic and thermodynamic properties of the system. Therefore, the MCE in MoTe$_2$-EuO is obtained through constant temperature (isothermal) calculations of entropy changes $-\Delta S_{eM}^{s_z}$ between the entropy at zero MEF, and a final MEF as

$$-\Delta S_{eM}^{s_z} = S_{eM}^{s_z}(B_v = B_c = 0, T) - S_{eM}^{s_z}(B_v, B_c, T), \quad (5)$$

where we have ascribed the fact that $S_{lat}(T)$ is not affected by the MEFs so that it does not present changes as B_v and B_c vary. In case to obtain $-\Delta S_{eM}^{s_z} > 0$, we are in the presence of the direct MCE, that is, MoTe$_2$-EuO is capable to heat as B_v and B_c change. In the opposite case, when $-\Delta S_{eM}^{s_z} < 0$, the system presents an inverse MCE, and the sample cools down. This quantum-thermodynamic model provides an efficient and reliable approach to study spin-polarized properties of the proximity-induced MCE within both the Fermi-Dirac and the mean-field methods.

III. MAGNETOCALORIC REPONSE IN MoTe$_2$-EuO

In the electronic spectra of MoTe$_2$-EuO in Fig. 1, we have chosen two different Fermi levels to obtain the MCE as spin-polarized electromagnetic entropy changes $-\Delta S_{eM}^{s_z}$. These Fermi levels can be shifted by an overall gate field perpendicular to the TMD layer [1,48], allowing for a tunable MCE in MoTe$_2$-EuO. The first Fermi-level $\mu_1(T = 0) = E_{F1} = -1.17$ eV is along the valence band, taking energies mainly from K and K' valleys, whereas $\mu_2(T = 0) = E_{F2} = 0.2$ eV crosses the K-Γ-K' $\boldsymbol{k}$ path of the BZ, capturing additional valleys in the conduction band [see Fig. 1(a)]. As we use EuO in our calculations, it is important to know that their Curie temperature $T_C = 69$ K [31,49] can be larger when EuO is doped [50] or when placed in close proximity to a 2D layer, such as graphene [51]. The latter shows that magnetic proximity effects including EuO are suitable for the study of magnetocaloric responses considering temperatures beyond the T_C of EuO.

Figure 2 shows $-\Delta S_{eM}^{s_z}$ as a function of temperature for MoTe$_2$-EuO considering μ_1 and μ_2 and different values of temperature-independent exchange fields B_v and B_c. Note that the units for the vertical axis $(\mu\text{eV/K}) \simeq (\text{J kg}^{-1}\text{ K}^{-1})$ as the MoTe$_2$ unit cell in the 3OTB model has one Mo atom, and one mole of Mo weighs $\simeq 0.096$ Kg. Clearly, the MCE has very different behavior for both Fermi levels in Fig. 2. At $\mu_1 = -1.17$ eV in Fig. 2(a), the MCE shows nearly
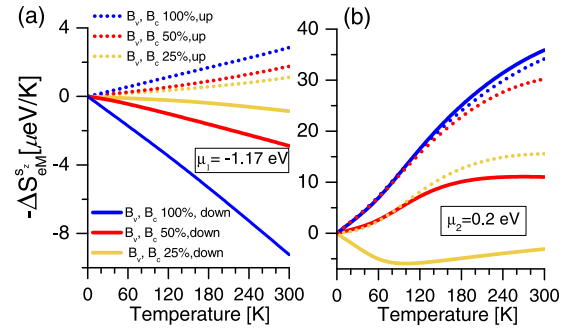

FIG. 2. Spin-polarized $-\Delta S_{eM}^{s_z}$ as a function of T for MoTe$_2$-EuO when $\lambda_R = 0$, B_v, and B_c are 25% (yellow), 50% (red), and 100% (blue) within the Fermi-Dirac statistics. The chemical potential is set to (a) $\mu_1 = -1.17$ eV, and (b) $\mu_2 = 0.2$ eV.

a linear response as temperature increases, is strongly spin polarized for all MEF values, and it is seen that weaker MEFs result in reduced MCE. At this Fermi level, the spin-up polarized entropy changes are $-\Delta S_{eM}^{\uparrow} > 0$, contributing to heat the system, whereas for spin-down $-\Delta S_{eM}^{\downarrow} < 0$, cooling down the sample up to room temperature. This dual behavior for the MCE is fully related to the connection of the DOS and entropy $S_{eM}^{s_z}$ from Eq. (4). The DOS with spin-up component $D^{\uparrow}$ of the suspended MoTe$_2$ monolayer is larger than all other $D^{\uparrow}$s with MEFs different from zero, that is $D^{\uparrow}(\mu_1, B_v = 0, B_c = 0) > D^{\uparrow}(\mu_1, B_v \neq 0, B_c \neq 0)$. This gives a positive MCE from Eq. (5), whereas the opposite is true for $D^{\downarrow}$ at μ_1. As we will see later, these results are qualitatively preserved up to the T_C of EuO within the mean-field approximation (MFA).

In striking contrast, when the Fermi-level $\mu_2 = 0.2$ eV is along the conduction band as shown in Fig. 2(b), $-\Delta S_{eM}^{s_z}$s are nonlinearly spin polarized and one order of magnitude larger than at μ_1. For MEF of 100% (blue lines), $-\Delta S_{eM}^{s_z}$s start to be spin polarized for $T > 120$ K, heating the sample for both spins. As B_v and B_c decrease to 50%, both spin-polarized components of $-\Delta S_{eM}^{s_z}$ (red lines) still heats up, and $-\Delta S_{eM}^{\uparrow}$ (dotted red line) has the same value as the entropy changes for 100% of EuO up to $T \approx 90$ K because the L function [Eq. (4)] captures the same amount of states of the DOS. $-\Delta S_{eM}^{s_z}$ for MEF of 25% are fully spin polarized from 0 to 300 K, $-\Delta S_{eM}^{\uparrow}$ (yellow dotted line) heats up, whereas $-\Delta S_{eM}^{\downarrow}$ (yellow solid line) cools down. This behavior is fully related to the magnitudes of D^{s_z} as we describe below.

We calculated $-\Delta S_{eM}^{s_z}$ as a function of the chemical potential for 100% and 25% of EuO, and selecting two values of temperature (below and above the T_C of EuO). Figure 3(a) shows $-\Delta S_{eM}^{s_z}$ at $T = 65$ K and Fig. 3(b) at $T = 150$ K. Because the MEFs compete with the intrinsic SOC of the 2D MoTe$_2$ monolayer, $-\Delta S_{eM}^{s_z}$ is strongly spin polarized as a function of μ for both values of T and MEF strengths of EuO. For both temperatures and in the range of energies of the valence valley polarization (-1.5 eV $\lesssim \mu \lesssim -0.9$ eV), $-\Delta S_{eM}^{s_z}$ for full EuO MEF (blue lines) show positive (heating) and negative (cooling) peaks near where D^{s_z}s present maxima, i.e., at $\mu \simeq -1.5$ eV for suspended MoTe$_2$ and at $\mu \simeq -1.3$ eV
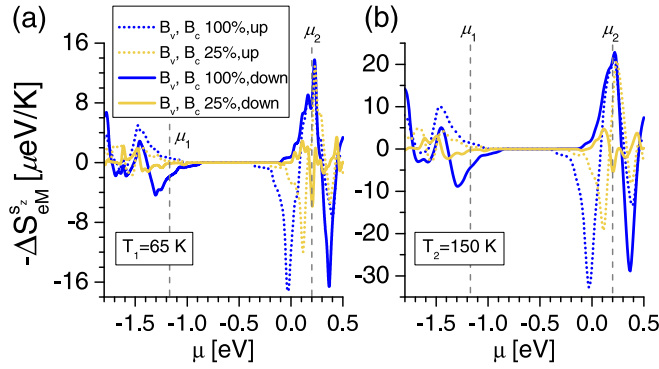
FIG. 3. Spin-polarized $-\Delta S_{eM}^{s_z}$ as a function of μ for MoTe$_2$-EuO when $\lambda_R = 0$ and B_v, B_c are 25% (yellow) and 100% (blue). The temperature is set to (a) $T_1 = 65$ K below the T_C of EuO, and (b) $T = 150$ K above the T_C of EuO. The dashed vertical lines indicate the chemical potentials used in Fig. 2.
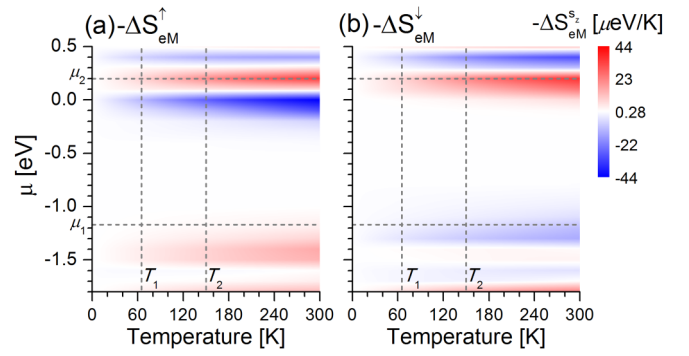

FIG. 4. Contour plots for $-\Delta S_{eM}^{s_z}$ as a function of the chemical potential and temperature for MoTe$_2$-EuO when $\lambda_R = 0$ and B_v and B_c are 100%, (a) spin up and (b) spin down. Horizontal gray dashed lines indicate the two different μ values for $-\Delta S_{eM}^{s_z}$ calculations in Fig. 2. Vertical gray dashed lines show temperatures used in Fig. 3, $T_1 = 65$, $T_2 = 150$ K. The color bar indicates positive (negative) entropy changes as a red (blue) gradient. Note that the units for $-\Delta S_{eM}^{s_z}$ (μeV/K) $\simeq$ (J kg^{-1}K^{-1}) are equivalent within our 3OTB model.

for $D^{\downarrow}$ of 100% EuO, respectively, see Figs. 1(b) and 1(c). $-\Delta S_{eM}^{s_z}$ vanishes in the band-gap region of the combined MoTe$_2$-EuO system (-0.9 eV $\lesssim \mu \lesssim -0.4$ eV) for both values of T and MEFs strengths as there are not available states in the energy spectra.

For Fermi levels in the conduction bands (-0.4 eV $\lesssim \mu \lesssim 0.5$ eV), there are large positive and negative peaks for $-\Delta S_{eM}^{s_z}$. For 100% of EuO, a clear negative peak is near $\mu \simeq 0$ due to the maxima of $D^{\uparrow}$ at this Fermi level [Fig. 1(c)]. Two other positive peaks are almost nonspin polarized about $\mu_2 = 0.2$ eV [in agreement with Fig. 3(b)] as D^{s_z} of the suspended MoTe$_2$ monolayer presents maxima near this energy. Two negative peaks are about $\mu \simeq 0.4$ eV, where $D^{\downarrow}$ shows a large peak, whereas $D^{\uparrow}$ is reduced, giving different $-\Delta S_{eM}^{s_z}$ values near this Fermi level for 100% of EuO. Note that $-\Delta S_{eM}^{s_z}$ is about two times larger for $T = 150$ K because the L function in Eq. (4) captures more states of the DOS when temperature increases. As the MEFs decrease to 25% of EuO, some $-\Delta S_{eM}^{s_z}$ conduction peaks are shifted from 100% of EuO and have opposite spin polarization at $\mu_2 = 0.2$ eV due to similar $D^{\downarrow}$ magnitudes for MoTe$_2$ with 25% of EuO [Fig. 1(b)].

Because the entropy changes for the MoTe$_2$-EuO heterostructure are highly dependent on the chemical potential and temperature, we present contour plots for the spin-polarized $-\Delta S_{eM}^{s_z}$ as a function of μ and T for EuO full MEF, $-\Delta S_{eM}^{\uparrow}$ in Fig. 4(a) and $-\Delta S_{eM}^{\downarrow}$ in Fig. 4(b). We can see that into the valence valley polarization energy zone ~ -1.3 to -1 eV, the system is capable to heat for spin up, and cools for spin down. As higher Fermi levels are reached in the conduction bands ($\mu \gtrsim -0.2$ eV), $-\Delta S_{eM}^{\uparrow}$ cools, then heats, and again cools, whereas $-\Delta S_{eM}^{\downarrow}$ heats and then cools. Accordingly, by tuning the Fermi level across the structure one could modulate the spin-polarized MCE in the MoTe$_2$-EuO system to cooling or simultaneously heating through the anomalous Hall effect [37], for example.

The broken spatial symmetry generated by the proximity with the EuO substrate generates an interfacial Rashba field [41,42,52–54] that produces in-plane spin contributions s_x and s_y on the MoTe$_2$ 2D monolayer [15]. We have incorporated the

Rashba field in our calculations for exchange fields of 100% and 25% as shown in Fig. 5 for $-\Delta S_{eM}^{R}$ as a function of T. In order to compare the effect of the Rashba field, we have used the previous MCE results when $\lambda_R = 0$ (Fig. 2) through $-\Delta S_{eM}^{\uparrow+\downarrow} = -\Delta S_{eM}^{\uparrow} + (-\Delta S_{eM}^{\downarrow})$.

Figure 5(a) shows that at $\mu_1 = -1.17$ eV, the Rashba field produces a negative MCE (cooling) for both EuO MEF strengths and linearly enhances the entropy changes for EuO full MEF (symbol green line). At $\mu_2 = 0.2$ eV in Fig. 5(b), the entropy changes for 100% of EuO have the same values with and without the Rashba field up to near the T_C of EuO. As temperature increases, the Rashba field does not improve the entropy changes up to room temperature. A contrasting behavior is seen for MEFs of 25% of EuO in which the entropy changes present different values for all temperatures, and the Rashba field enhanced it starting in $T \approx 100$ K. These results suggest that for full EuO MEFs, the in-plane spin components are stronger in the valence band than in the conduction band
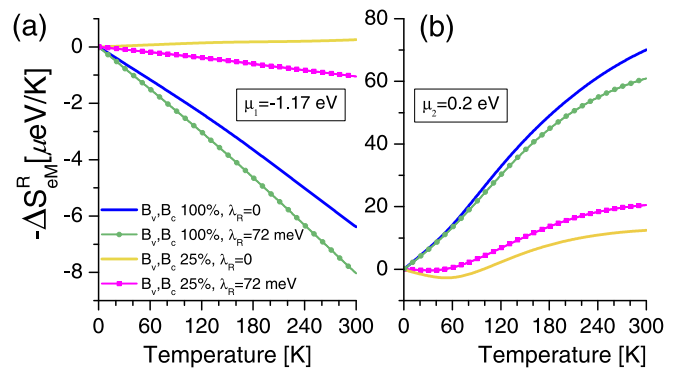

FIG. 5. $-\Delta S_{eM}^{R}$ as a function of T for (a) $\mu_1 = -1.17$ eV and (b) $\mu_2 = 0.2$ eV for MoTe$_2$-EuO when $\lambda_R = 0$ (solid lines), $\lambda_R = 72$ meV (symbol lines), and B_v, and B_c are 25% (yellow and pink), and 100% (green and blue) of EuO.
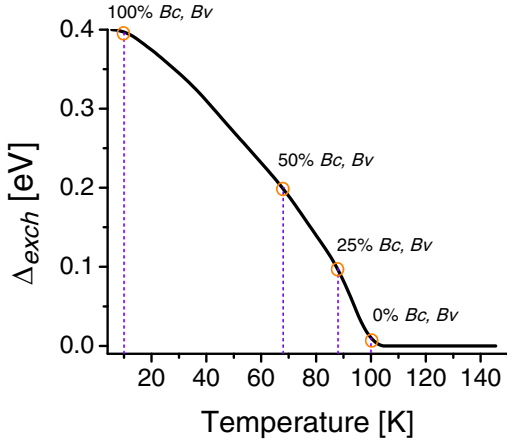
FIG. 6. Δ_{exch} as a function of temperature when $\lambda_R = 0$ for MoTe$_2$-EuO with B_v and B_c values from Fig. 1. We have fixed the Curie temperature for the MoTe$_2$-EuO system at $T_C' = 100$ K because the intrinsic $T_C = 69$ K of EuO changes when in proximity to a 2D material [51]. Vertical violet lines indicate selected T values from Ref. [32], and orange circles highlight the $\Delta_{exch} - T$ correspondence for exchange fields B_c and B_v.

as temperature increases, generating an enhanced MCE when the Rashba field is present.

IV. MEAN-FIELD APPROXIMATION

In order to obtain the entropy changes with the temperature-dependent exchange fields B_v and B_c, we present mean-field calculations for the MoTe$_2$-EuO system considering the previous spin-polarized DOS results and the experimental data for magnetization as a function of temperature for EuO thin films [32]. Figure 6 shows the energy difference $\Delta_{exch} = |E^\uparrow(B_v, B_c) - E^\downarrow(B_v, B_c)|$ as a function of T for the larger peaks in the conduction band with different B_v and B_c values we have plotted in the DOS of Figs. 1(b) and 1(c), and considering a new Curie temperature for the combined MoTe$_2$-EuO system of $T_C' = 100$ K. When we have 100% of the exchange field values, we obtain $\Delta_{exch} = 0.4$ eV at low-temperature $T = 10$ K. For 50% and 25% of B_v and B_c, Δ_{exch} decreases as T increases, reaching a vanishing value for $T \geqslant 100$ K as the MoTe$_2$ monolayer presents a paramagnetic behavior when decoupled from the EuO substrate. With this $\Delta_{exch}(T)$ relation, now we can calculate new entropies of the form $S_{eM}^{s_z}[\Delta_{exch}(T)]$. These new entropies are obtained from Eq. (4) by using the calculated DOS from Fig. 1 and fixing the temperature in the L function to the values showed by vertical violet lines in Fig. 6. Within this approximation, we obtain a discrete set of three spin-polarized entropies (100%, 50%, and 25% of B_v and B_c) where each one of them includes the $\Delta_{exch} - T$ correspondence from Fig. 6 indicated with orange circles. Then, we interpolate these discrete entropy values to get continuous entropies as a function of temperature for selected Fermi levels, which allow us to get the desired entropy changes within the MFA.

Figure 7 shows the entropy changes $-\Delta S_{eM}^{s_z}$ as a function of temperature in the MFA at the Fermi levels we have previously used. Clearly, the $-\Delta S_{eM}^{s_z}$ shapes are different as
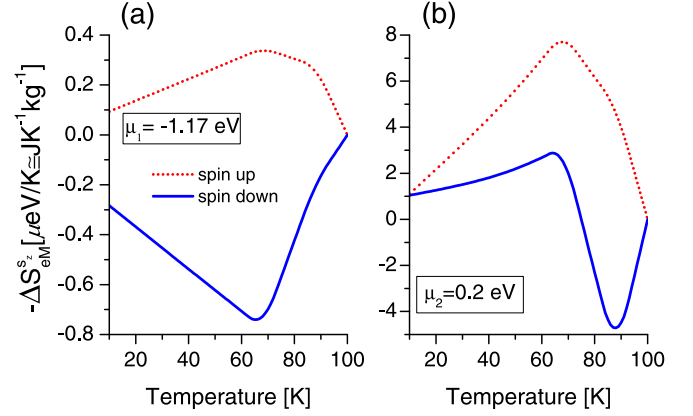

FIG. 7. $-\Delta S_{eM}^{s_z}$ as a function of T in the mean-field approximation for (a) $\mu_1 = -1.17$ eV and (b) $\mu_2 = 0.2$ eV for MoTe$_2$-EuO when $\lambda_R = 0$ with spin up (dotted red lines) and spin down (solid blue lines).

presented in Fig. 2 because the induced exchange fields B_v and B_c now are temperature dependent. For Fermi-level μ_1 in Fig. 7(a), $-\Delta S_{eM}^\uparrow$ is positive (heating) whereas $-\Delta S_{eM}^\downarrow$ is negative (cooling) for the whole temperature range, and both spin-polarized entropy changes linearly increase up to $T \approx$ 65 K as also seen in Fig. 2(a). Both components show the expected magnetic transition near the T_C of EuO where absolute maxima are seen, then they decrease as temperature increases. At Fermi-level μ_2 in Fig. 7(b), both spin components show the magnetic transition near the T_C of EuO where two positive maxima occur near $T_C \approx 70$ K. The spin-up component is positive for all Ts [similar to $-\Delta S_{eM}^\uparrow$ in Fig. 2(b)], whereas the spin-down component is positive up to $T \approx 80$ where it presents a sign change, then increases with negative values where a minimum is present about $T \approx 90$ K, and finally it decreases with T. This behavior is different from $-\Delta S_{eM}^\downarrow$ of Fig. 2(b) because the DOS with spin-down component $D^\downarrow$ and 25% of B_v and B_c is larger than $D^\downarrow$ for the suspended
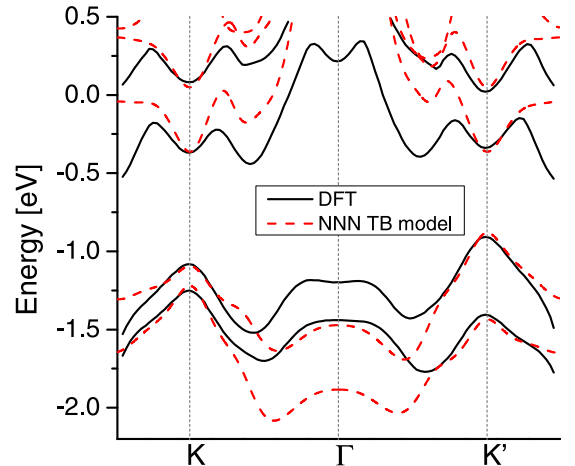

FIG. 8. Comparison for the band structures of MoTe$_2$-EuO with different theoretical approaches as indicated. Red dashed lines correspond to the NNN tight-binding model, and black lines are DFT calculations [15].

MoTe$_2$, yielding to negative entropy changes for $T > 80$ K. Therefore, the spin-down polarized component can heats for $T \lesssim 80$ K and cools for $T \geqslant 80$ K, giving account of a mixed induced magnetocaloric effect at the Fermi-level μ_2 in the MoTe$_2$-EuO system.

V. CONCLUSIONS

Time-reversal symmetry breaking on the 2D MoTe$_2$ monolayer because of induced EuO magnetic exchange fields result in density of states variations, producing large spin-polarized entropy changes across the valley splitting energy-momentum space, yielding to the magnetocaloric effect in the combined MoTe$_2$-EuO system. By gating the heterostructure, tunable spin-dependent heating and/or cooling can be achieved in the valence and conduction energy zones, improving it when the Rashba field is taken into account in the valence band. Fermi-Dirac statistics is in agreement with mean-field calculations up to the intrinsic Curie temperature of EuO, and we would expect larger Curie temperatures for MoTe$_2$-EuO in a similar way as for graphene on EuO [51]. The proximity-induced magnetocaloric effect in semiconducting MoTe$_2$ on EuO reveals spin-dependent quantum-thermodynamic responses that could be used in the design of novel atomistic cooling technologies.

APPENDIX: TIGHT-BINDING AND DFT MODELS

Figure 8 shows a comparison between the tight-binding model we use in our calculations and the density functional band structure for MoTe$_2$-EuO with full exchange field values $B_v = 170$ and $B_c = 206$ meV and $\lambda_R = 72$ meV from Ref. [15]. We see excellent agreement between the tight-binding Hamiltonian [Eq. (1)] and the density functional model [15] near the K and K' valleys in the valence and conduction bands. Our *magnetized* 3OTB model provides an excellent description for energies ~ 300 meV from the valence-band edge, for example, corresponding to hole dopings on the order of $\sim 10^{12}$ cm^{-2}, similar to experimental doping values [55].

[1] I. Žutić, A. Matos-Abiague, B. Scharf, H. Dery, and K. Belashchenko, Mater. Today **22**, 85 (2019).

[2] A. K. Geim and I. V. Grigorieva, Nature (London) **499**, 419 (2013).

[3] O. V. Yazyev and A. Kis, Mater. Today **18**, 20 (2015).

[4] P. Ajayan, P. Kim, and K. Banerjee, Phys. Today **69**(9), 38 (2016).

[5] G.-B. Liu, D. Xiao, Y. Yao, X. Xu, and W. Yao, Chem. Soc. Rev. **44**, 2643 (2015).

[6] S. Manzeli, D. Ovchinnikov, D. Pasquier, O. V. Yazyev, and A. Kis, Nat. Rev. Mater. **2**, 17033 (2017).

[7] D. Xiao, G.-B. Liu, W. Feng, X. Xu, and W. Yao, Phys. Rev. Lett. **108**, 196802 (2012).

[8] G. Aivazian, Z. Gong, A. M. Jones, R.-L. Chu, J. Yan, D. G. Mandrus, C. Zhang, D. Cobden, W. Yao, and X. Xu, Nat. Phys. **11**, 148 (2015).

[9] C. Zhao, T. Norden, P. Zhang, P. Zhao, Y. Cheng, F. Sun, J. P. Parry, P. Taheri, J. Wang, Y. Yang, T. Scrace, K. Kang, S. Yang, G.-x. Miao, R. Sabirianov, G. Kioseoglou, W. Huang, A. Petrou, and H. Zeng, Nat. Nanotechnol. **12**, 757 (2017).

[10] D. Zhong, K. L. Seyler, X. Linpeng, R. Cheng, N. Sivadas, B. Huang, E. Schmidgall, T. Taniguchi, K. Watanabe, M. A. McGuire, W. Yao, D. Xiao, K.-M. C. Fu, and X. Xu, Sci. Adv. **3**, e1603113 (2017).

[11] K. L. Seyler, D. Zhong, B. Huang, X. Linpeng, N. P. Wilson, T. Taniguchi, K. Watanabe, W. Yao, D. Xiao, M. A. McGuire, K.-M. C. Fu, and X. Xu, Nano Lett. **18**, 3823 (2018).

[12] C. Zou, C. Cong, J. Shang, C. Zhao, M. Eginligil, L. Wu, Y. Chen, H. Zhang, S. Feng, J. Zhang *et al.*, Nano Res. **11**, 6252 (2018).

[13] Y. Li, J. Ludwig, T. Low, A. Chernikov, X. Cui, G. Arefe, Y. D. Kim, A. M. van der Zande, A. Rigosi, H. M. Hill, S. H. Kim, J. Hone, Z. Li, D. Smirnov, and T. F. Heinz, Phys. Rev. Lett. **113**, 266804 (2014).

[14] D. MacNeill, C. Heikes, K. F. Mak, Z. Anderson, A. Kormányos, V. Zólyomi, J. Park, and D. C. Ralph, Phys. Rev. Lett. **114**, 037401 (2015).

[15] J. Qi, X. Li, Q. Niu, and J. Feng, Phys. Rev. B **92**, 121403(R) (2015).

[16] T. Norden, C. Zhao, P. Zhang, R. Sabirianov, A. Petrou, and H. Zeng, Nat. Commun. **10**, 4163 (2019).

[17] J. R. Gómez, R. F. Garcia, A. D. M. Catoira, and M. R. Gómez, Renewable Sustainable Energy Rev. **17**, 74 (2013).

[18] C. W. Miller, D. D. Belyea, and B. J. Kirby, J. Vac. Sci. Technol. A **32**, 040802 (2014).

[19] V. Franco, J. Blázquez, J. Ipus, J. Law, L. Moreno-Ramírez, and A. Conde, Prog. Mater. Sci. **93**, 112 (2018).

[20] P. Von Ranke, N. De Oliveira, B. Alho, E. Plaza, V. De Sousa, L. Caron, and M. Reis, J. Phys.: Condens. Matter **21**, 056004 (2009).

[21] T. Chakraborty and C. Mitra, J. Phys.: Condens. Matter **31**, 475802 (2019).

[22] M. Zhitomirsky and A. Honecker, J. Stat. Mech.: Theory Exp. (2004) P07012.

[23] M. E. Zhitomirsky, Phys. Rev. B **67**, 104421 (2003).

[24] A. Honecker and S. Wessel, Physica B **378**, 1098 (2006).

[25] R. Skomski, C. Binek, T. Mukherjee, S. Sahoo, and D. J. Sellmyer, J. Appl. Phys. **103**, 07B329 (2008).

[26] T. Mukherjee, S. Sahoo, R. Skomski, D. J. Sellmyer, and C. Binek, Phys. Rev. B **79**, 144406 (2009).

[27] M. Reis, J. Appl. Phys. **113**, 243901 (2013).

[28] M. Reis, Appl. Phys. Lett. **101**, 222405 (2012).

[29] T. Diffo, A. Fotue, S. Kenfack, R. K. Tsiaze, E. Baloitcha, and M. Hounkonnou, Phys. Lett. A **385**, 126958 (2021).

[30] T. Hashimoto, T. Numasawa, M. Shino, and T. Okada, Cryogenics **21**, 647 (1981).

[31] K. Ahn, A. Pecharsky, K. Gschneidner, Jr., and V. Pecharsky, J. Appl. Phys. **97**, 063901 (2005).

[32] P. Lampen-Kelley, R. Madhogaria, N. S. Bingham, M. H. Phan, P. M. S. Monteiro, N.-J. Steinke, A. Ionescu, C. H. W. Barnes, and H. Srikanth, Phys. Rev. Mater. **5**, 094404 (2021).

[33] N. Li, J. Zhang, Y. Xue, T. Zhou, and Z. Yang, Phys. Chem. Chem. Phys. **20**, 3805 (2018).

[34] C. Maes and K. Netočný, J. Stat. Phys. **110**, 269 (2003).

[35] D. Andrieux, P. Gaspard, S. Ciliberto, N. Garnier, S. Joubaud, and A. Petrosyan, Phys. Rev. Lett. **98**, 150601 (2007).

[36] Z. Gholami and F. Khoeini, Sci. Rep. **11**, 15320 (2021).

[37] T. Habe and M. Koshino, Phys. Rev. B **96**, 085411 (2017).

[38] B. Scharf, G. Xu, A. Matos-Abiague, and I. Žutić, Phys. Rev. Lett. **119**, 127403 (2017).

[39] G.-B. Liu, W.-Y. Shan, Y. Yao, W. Yao, and D. Xiao, Phys. Rev. B **88**, 085433 (2013).

[40] M. Luo, Phys. Rev. B **100**, 195410 (2019).

[41] N. Cortés, O. Ávalos-Ovando, L. Rosales, P. A. Orellana, and S. E. Ulloa, Phys. Rev. Lett. **122**, 086401 (2019).

[42] N. Cortés, O. Ávalos-Ovando, and S. E. Ulloa, Phys. Rev. B **101**, 201108(R) (2020).

[43] O. Ávalos-Ovando, D. Mastrogiuseppe, and S. E. Ulloa, Phys. Rev. B **94**, 245429 (2016).

[44] O. Ávalos-Ovando, D. Mastrogiuseppe, and S. E. Ulloa, Phys. Rev. B **93**, 161404(R) (2016).

[45] A. M. Alsharari, M. M. Asmar, and S. E. Ulloa, Phys. Rev. B **97**, 241104(R) (2018).

[46] Q. Zhang, S. A. Yang, W. Mi, Y. Cheng, and U. Schwingenschlögl, Adv. Mater. **28**, 959 (2016).

[47] N. Cortés, O. Negrete, F. J. Peña, and P. Vargas, Sci. Rep. **11**, 22000 (2021).

[48] P. Lazić, K. D. Belashchenko, and I. Žutić, Phys. Rev. B **93**, 241401(R) (2016).

[49] D. V. Averyanov, A. M. Tokmachev, O. E. Parfenov, I. A. Karateev, I. S. Sokolov, A. N. Taldenkov, M. S. Platunov, F. Wilhelm, A. Rogalev, and V. G. Storchak, Appl. Surf. Sci. **488**, 107 (2019).

[50] H. Ott, S. J. Heise, R. Sutarto, Z. Hu, C. F. Chang, H. H. Hsieh, H.-J. Lin, C. T. Chen, and L. H. Tjeng, Phys. Rev. B **73**, 094407 (2006).

[51] D. V. Averyanov, I. S. Sokolov, A. M. Tokmachev, O. E. Parfenov, I. A. Karateev, A. N. Taldenkov, and V. G. Storchak, ACS Appl. Mater. Interfaces **10**, 20767 (2018).

[52] C. L. Kane and E. J. Mele, Phys. Rev. Lett. **95**, 226801 (2005).

[53] H. Ochoa and R. Roldán, Phys. Rev. B **87**, 245421 (2013).

[54] T. Frank, P. Högl, M. Gmitra, D. Kochan, and J. Fabian, Phys. Rev. Lett. **120**, 156402 (2018).

[55] S. Pan, F. Ceballos, M. Z. Bellus, P. Zereshki, and H. Zhao, 2D Mater. **4**, 015033 (2016).